

1 **Fast retrograde access to projection neuron circuits underlying vocal learning in songbirds**

2

3 *Düring DN^{1,2,3}, Dittrich F³, Rocha MD³, Tachibana RO⁴, Mori C⁴, Okanoya K⁴, Boehringer R^{1,2},
4 Ehret B^{1,2}, Grewe BF^{1,2}, Rauch M⁵, Paterna JC⁵, Kasper R⁶, Gahr M³, and Hahnloser RHR^{1,2}

5

6 ¹Institute of Neuroinformatics, University of Zürich/ETH Zürich, Zurich, Switzerland

7 ²Neuroscience Center Zurich (ZNZ), Zurich, Switzerland

8 ³Department of Behavioural Neurobiology, Max Planck Institute for Ornithology, Seewiesen,
9 Germany

10 ⁴Department of Life Sciences, The University of Tokyo, Tokyo, Japan

11 ⁵Viral Vector Facility (VVF) of the Neuroscience Center Zurich (ZNZ), Zurich, Switzerland

12 ⁶Imaging Center of the Max Planck Institute of Neurobiology, Munich, Germany.

13 *corresponding author email: dduering@ethz.ch

14

15 **Summary**

16 Understanding the structure and function of neural circuits underlying speech and language is a vital
17 step towards better treatments for diseases of these systems. Songbirds, among the few animal orders
18 that share with humans the ability to learn vocalizations from a conspecific, have provided many
19 insights into the neural mechanisms of vocal development. However, research into vocal learning
20 circuits has been hindered by a lack of tools for rapid genetic targeting of specific neuron populations
21 to meet the quick pace of developmental learning. Here, we present a new viral tool that enables fast
22 and efficient retrograde access to projection neuron populations. In zebra finches, Bengalese finches,
23 canaries, and mice, we demonstrate fast retrograde labeling of cortical or dopaminergic neurons. We
24 further demonstrate the suitability of our construct for detailed morphological analysis, for *in vivo*
25 imaging of calcium activity, and for multicolor brainbow labeling.

26

27

28

29 **Introduction**

30 Speech and language disorders affect millions of children worldwide¹. These disorders are associated
31 with a number of pathologies, including autism spectrum² and attention deficit hyperactivity
32 disorders³, but they also occur in otherwise normally developing children. The causes of speech and
33 language disorders are poorly understood, but abnormal brain structure likely plays a crucial role⁴□.
34 Interestingly, neither mice, the most common animal model for pre-clinical studies, nor our closest
35 relatives, non-human primates, share the human ability to learn vocalizations by imitating a
36 conspecific⁵. Songbirds, on the other hand, are gifted vocal learners and display many parallels with
37 speech acquisition in humans⁶□. Therefore, songbirds provide an excellent model system to examine
38 the neural circuits associated with speech development. Songbird circuit research remains, however,
39 limited by the current lack of transgenic animal lines and proper neurogenetic tools.

40 The virally mediated delivery of genetic cargo to a specific neuron population is a highly valuable
41 approach for probing anatomy and circuit function. By entering at axon terminals, retrograde viral
42 vectors can specifically transduce projection neuron populations and provide direct access to the
43 wiring and function of the brain^{7,8}. Unfortunately, viral vectors are not easily transferable between
44 model species. For example, rabies and canine adenovirus (CAV), the most commonly used
45 retrograde vectors in rodents, have never been shown to successfully infect avian tissue. Other
46 examples include adeno associated viral (AAV) vectors that are commonly used in rodents and other
47 mammals, but suffer from major limitations in accessing songbird projection neurons⁹⁻¹⁵.

48 The limitations of the AAV vectors so far applied for retrograde access to songbird projection neurons
49 are four-fold. First, these AAV vectors result in low transduction success rates, with only 18% to 43%
50 of intracerebral injections resulting in successful transgene expression⁹. Second, their transduction of
51 projection neurons is sparse, resulting in transgene expression in small portions of the targeted
52 populations^{9,11}. This limitation makes these tools incompatible with studies requiring genetic
53 manipulations of a majority of neurons among a given type. The third limitation is weak transgene
54 expression^{9,13}. For example, when used to induce fluorescent protein expression, the resulting limited

55 dendritic and axonal labeling^{9,13} makes current retrograde tools unsuitable for morphological studies.
56 Finally, the fourth limitation of the current AAV vectors is that they require long incubation periods
57 of at least 4 to 6 weeks (and up to 6 months) post-injection until transgene expression becomes
58 detectable^{10,11,13}. Such long incubation periods typically hinder any vocal development studies in
59 zebra finches (*Taeniopygia guttata*), the most common songbird model species in neuroscience. This
60 is because zebra finches undergo short song learning phases during the critical period for vocal
61 learning. This period ends 90 days after hatching and is accompanied by fast brain rewiring¹⁶. The
62 rapid succession of vocal learning events in songbirds thus requires fast viral tools for circuit
63 investigations. To date, no viral vector has proven to efficiently target projection neurons of the
64 songbird brain resulting in robust transgene expression in a relevant time frame.

65 Here we present a fast and reliable retrograde viral tool for the songbird brain. Briefly, we combined
66 a self-complementary (sc) plasmid organization of a capsid variant of AAV-DJ, AAV-DJ/9¹⁷, and an
67 expression cassette under the transcriptional control of the human cytomegalovirus (hCMV)
68 promoter/immediate-early enhancer (IE) in combination with a chimeric intron (chI), resulting in
69 AAV vectors according to scAAV-2-DJ/9-hCMV-IE-chI-transgene-p(A) (Fig. 1a,b; Methods). In
70 several songbird species and in mice, we found that our viral construct is efficient in retrogradely
71 transducing projection neuron circuits within about one week after vector injection (Fig. 1c-o; Fig. 2).
72 Furthermore, our construct is suitable for detailed morphological investigations, for multi-color
73 brainbow imaging, and for *in-vivo* recordings of neural activity using fluorescent calcium sensors.

74

75

76

77

78

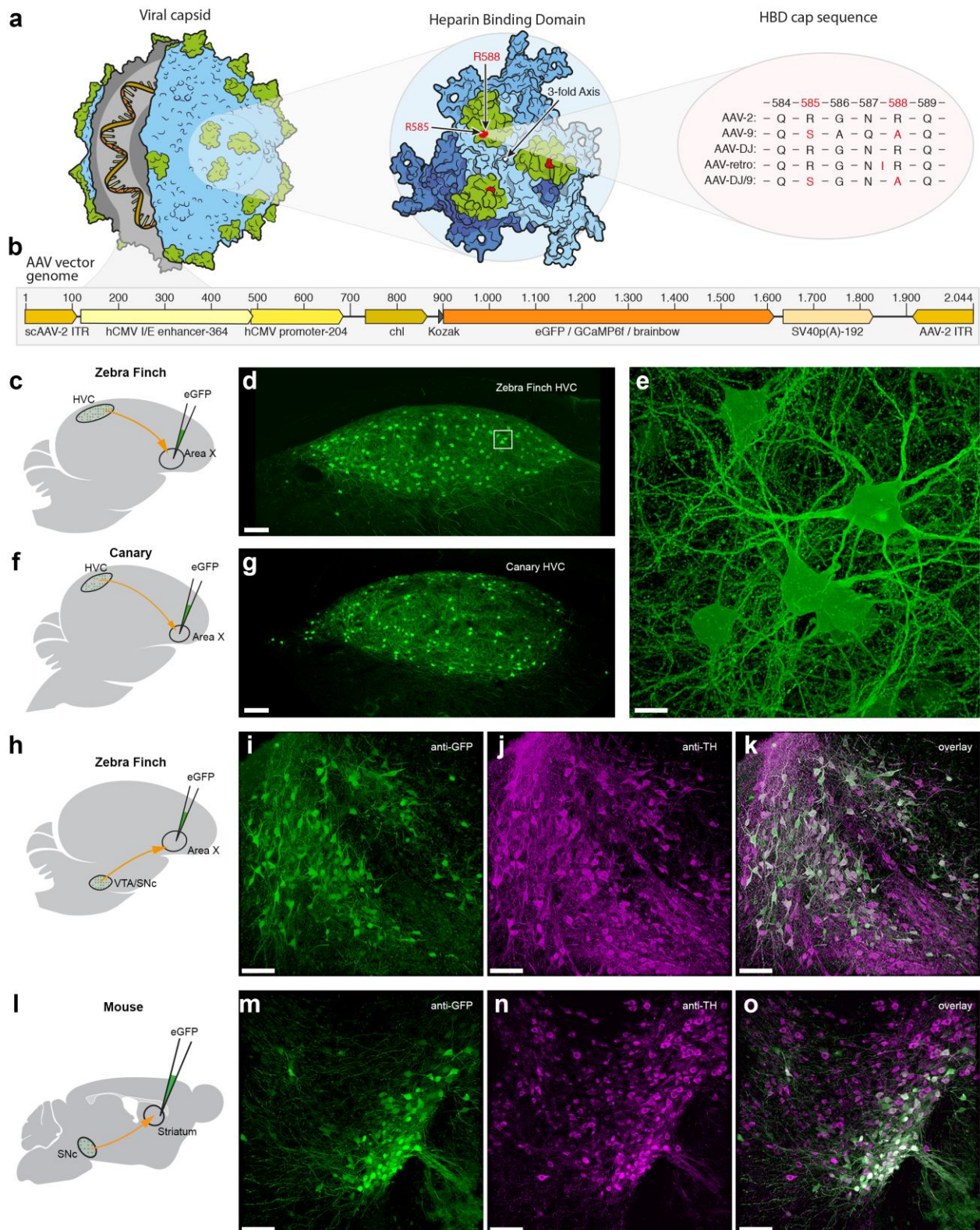
79

80 **Results**

81

82 **Fast and efficient retrograde transduction of songbird projection neurons**

83 First, we examined the transgene expression kinetics and stability of our viral construct. We assessed
84 expression performance in the corticostriatal connection from nucleus HVC (proper name) to Area
85 X. HVC, the songbird vocal premotor cortex analog, is a major hub during vocal learning, integrating
86 information from auditory¹⁸, dopaminergic¹⁵, and premotor¹⁹ afferents. HVC includes three major
87 neuron populations: local interneurons, HVC_{RA} neurons that project to the robust nucleus of the
88 arcopallium (RA), which innervates vocal and respiratory motor neurons, and HVC_X neurons that
89 project to Area X, the basal ganglia part of a cortico-basal ganglia-thalamic loop involved in song
90 learning²⁰. HVC_X neurons are analogous to mammalian corticostriatal projection neurons, which are
91 involved in motor learning in mammals²¹.



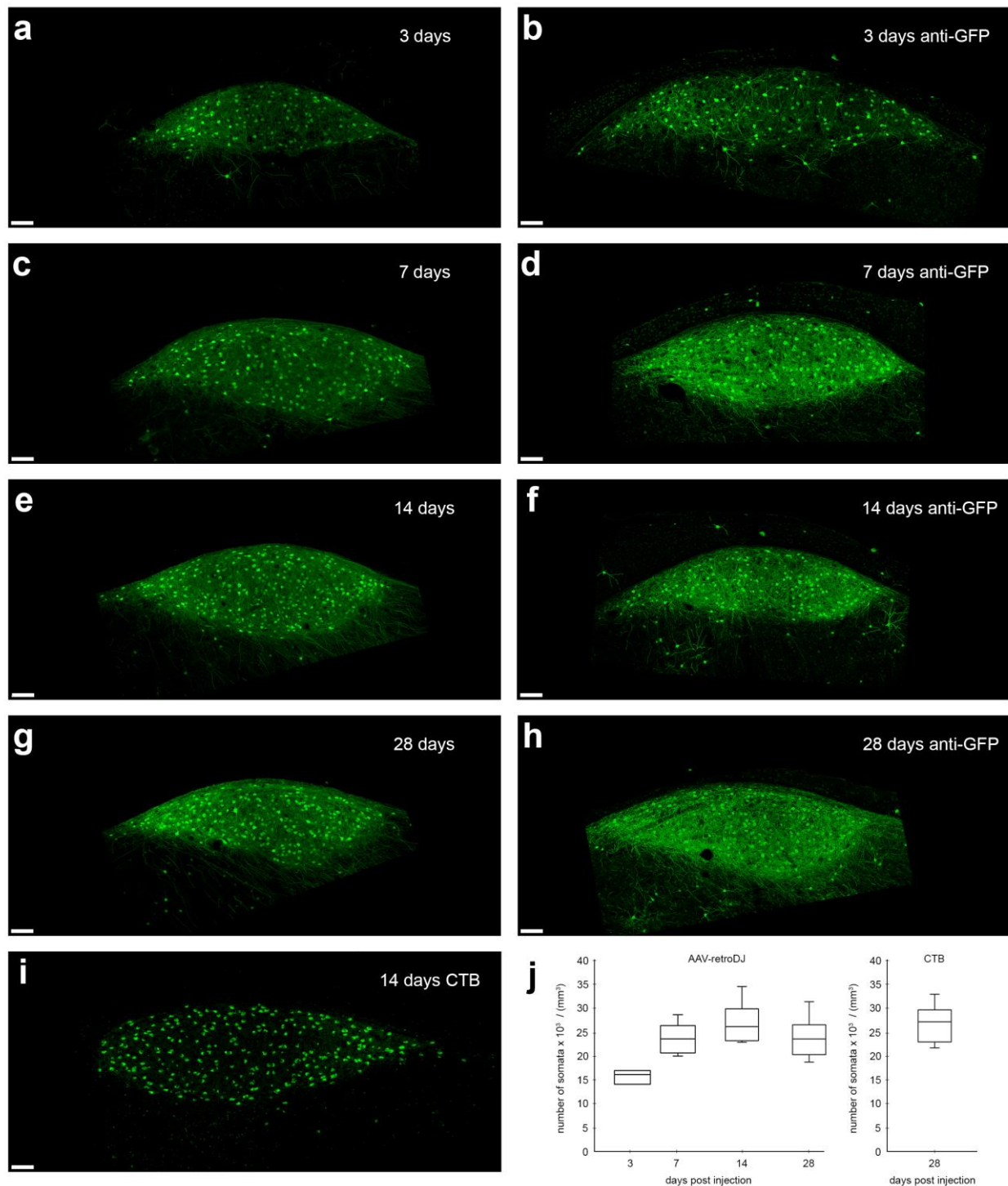
92

93 **Fig. 1 | AAV capsid and genome structure for efficient retrograde access to songbird and mouse**
 94 **projection and dopaminergic neurons.** **a**, Illustration of the AAV capsid, showing exposed surface
 95 proteins responsible for binding to the heparin sulfate proteoglycans (HSPG) receptor, thought to be
 96 important for cellular entry of the viral vector. Mutations of two crucial arginines in the heparin
 97 binding domain (HBD, highlighted in green) cap sequence at positions 585 and 588 (highlighted in
 98 red) reduce heparin binding affinity and potentially improve retrograde transport. Changes are shown

99 for four serotypes that have been used for or possess potential for retrograde transduction. **b**, AAV
100 vector genomes encoding diverse transgenes (orange region) including fluorescent proteins and the
101 calcium indicator GCaMP6f. Numbers on top indicate the base pair length and relative position of
102 encoded elements. Note that the actual size of the region encoding the transgene (orange) varies
103 depending on the respective protein. Brainbow stands for 3 separate AAV vector genomes encoding
104 either eGFP (enhanced green fluorescent protein), eCFP (enhanced cyan fluorescent protein), or
105 mRuby3 (red fluorescent protein). **c, f, h, i**, Schematics of the virus injection sites (green) and the
106 neuronal projections analyzed (red). **d, g**, Native fluorescence signal in retrogradely labeled HVC_X
107 neurons 7 days post virus delivery in zebra finch and in canary, respectively. **e**, Higher magnification
108 z-stack of the boxed region in d. Dopaminergic projection neurons in zebra finch (**i-k**) and mouse (**m-**
109 **o**) retrogradely labeled with our eGFP-construct, after immunostaining for anti-GFP (**i, m**) and anti-
110 Tyrosine hydroxylase (**j, n**). Scale bars 100 μm except e, 10 μm.

111

112 We found robust native fluorescence of eGFP in HVC_X neurons as early as 3 days post-injection of
113 scAAV-2-DJ/9-hCMV-I/E-chI-eGFP-p(A) into Area X (Fig. 2a,b). Abundant eGFP-filled neurons
114 could be seen within HVC throughout four different time points ranging from 3 to 28 days after
115 injection (Fig. 2a-h). Three days after injection, we detected eGFP labeling among 59% (15.56×10^3
116 somata/mm³, n=6 hemispheres) of HVC_X somata as compared to retrograde labeling with Cholera
117 Toxin B (CTB, 26.48×10^3 somata/mm³, n=8 hemispheres; Fig 2i,j), a commonly used and highly
118 efficient retrograde tracer in zebra finches²². Already 7 days post-injection, eGFP labeling density
119 (23.52×10^3 somata/mm³, n=8 hemispheres; Fig. 2c,j) was comparable with CTB labeling density,
120 hinting at a strikingly high transduction efficiency. Longer eGFP expression times of 14 and 28 days
121 did not further increase eGFP labeling densities (25.28×10^3 and 23.66×10^3 somata/mm³ respectively,
122 n=8 hemispheres per time point; Fig. 2e,g,j). These results suggest that the peak of native fluorescence
123 of eGFP expression is reached already 7 days post-delivery and that there is no obvious decay of
124 fluorescence or neurotoxicity for at least 4 weeks after injection.



125

126 **Fig. 2 | Retrograde transduction kinetics in zebra finch HVC_x neurons.** We find strong retrograde
127 expression of eGFP in Area-X projecting (HVC_x) neurons as early as 3 days after injection of scAAV-
128 2-DJ/9-hCMV-I/E-chI-eGFP-p(A) into Area X. Confocal images show native eGFP signal post-
129 delivery after **a**, 3 days; **c**, 7 days; **e**, 14 days; and **g**, 28 days; and **b**, **d**, **f**, **h**, their respective anti-GFP
130 immunostainings. **i**, Comparative image of retrogradely labeled HVC_x neurons 14 days after
131 injections of cholera toxin B (CTB, a retrograde neural tracer) into Area X. Note the strong eGFP
132 signal in neurites of virally labeled cells as early as 3 days as compared to the neural tracer. **j**, Number
133 of retrogradely labeled somata of HVC_x neurons after 3, 7, 14, and 28 days post-delivery into Area
134 X (based on native eGFP signal) compared to 14 days labeling with the retrograde tracer. Scale bars
135 100 μ m.

136

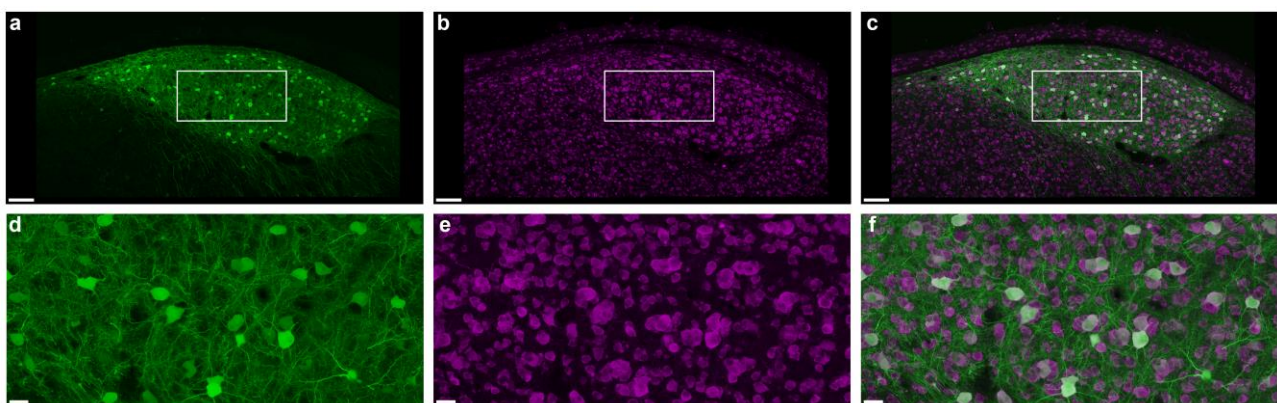
137 **Transduction success rate and specificity of retrograde projection-neuron labeling in songbirds**

138 We assessed the transduction success rate of our eGFP-construct, and found consistent transduction
139 of HVC_X neurons in 24 out of 24 single-injected hemispheres (n=12 birds) after a minimum of 7 days
140 after virus injection into Area X. For comparison, previous studies applying AAV vectors for
141 retrograde transduction in songbirds have reported overall successful transduction in as little as 18%
142 of virus injections (one brain pathway showing retrograde eGFP expression in 2 out of 11 injected
143 hemispheres)⁹. To date, we have not encountered a single injection of our eGFP-construct without
144 successful retrograde transduction of projection neurons after 7 days.

145 We further assessed the specificity of retrograde labeling. HVC and Area X are anatomically well
146 separated, which virtually excludes the possibility that viral particles passively diffuse from Area X
147 to HVC. In addition, the fact that this connection is unidirectional makes it safe to assume that all
148 labeled neurites in HVC belong to HVC_X neurons. Nonetheless, some studies report the possibility
149 of trans-synaptic spread of AAV vectors^{23,24}. To assess whether all labeled neurons are indeed HVC_X
150 neurons, and to exclude any potential mislabeling, we examined the morphological characteristics of
151 eGFP-labeled HVC neurons.

152 The three main HVC neuron classes are morphologically well described and can be separated based
153 on dendritic spine densities²⁵. HVC interneurons are mainly aspiny, HVC_{RA} projection neurons are
154 moderately spiny (0.21 ± 0.07 spines/ μm), and HVC_X neurons have the highest dendritic spine
155 densities (0.70 ± 0.13 spines/ μm). We analyzed 17 randomly chosen dendritic branches of various
156 lengths (total branch length of 396 μm) across n=4 adult male zebra finches (>7 days after injection).
157 A subset of histological brain sections was further subjected to anti-GFP immunolabeling to capture
158 any potentially low-transgene expressing cells. Analyzed dendritic branch fragments had dendritic
159 spine densities ranging from 0.47 to 1.75 spines/ μm (average 1.03 ± 0.35 spines/ μm , which compares
160 favorably with the previously reported 0.70 ± 0.13 spines/ μm ²⁵), indicating that eGFP-expressing

161 cells are most likely all HVC_X neurons. Albeit some overlap in spine density between X- and RA-
162 projecting cells, we did not encounter a single cell that was obviously either aspiny (interneuron) or
163 had a very low spine density (HVC_{RA} neurons).
164 To further exclude the possibility of unspecific transduction of non-neuronal cell types such as
165 astrocytes, we performed anti-neuronal protein HuC/HuD counterstains, a common neuronal marker.
166 We found that all examined eGFP-labeled cells were also labeled with HuC/HuD antibody (n=4
167 sections), confirming their neuronal identity (Fig. 3).



168

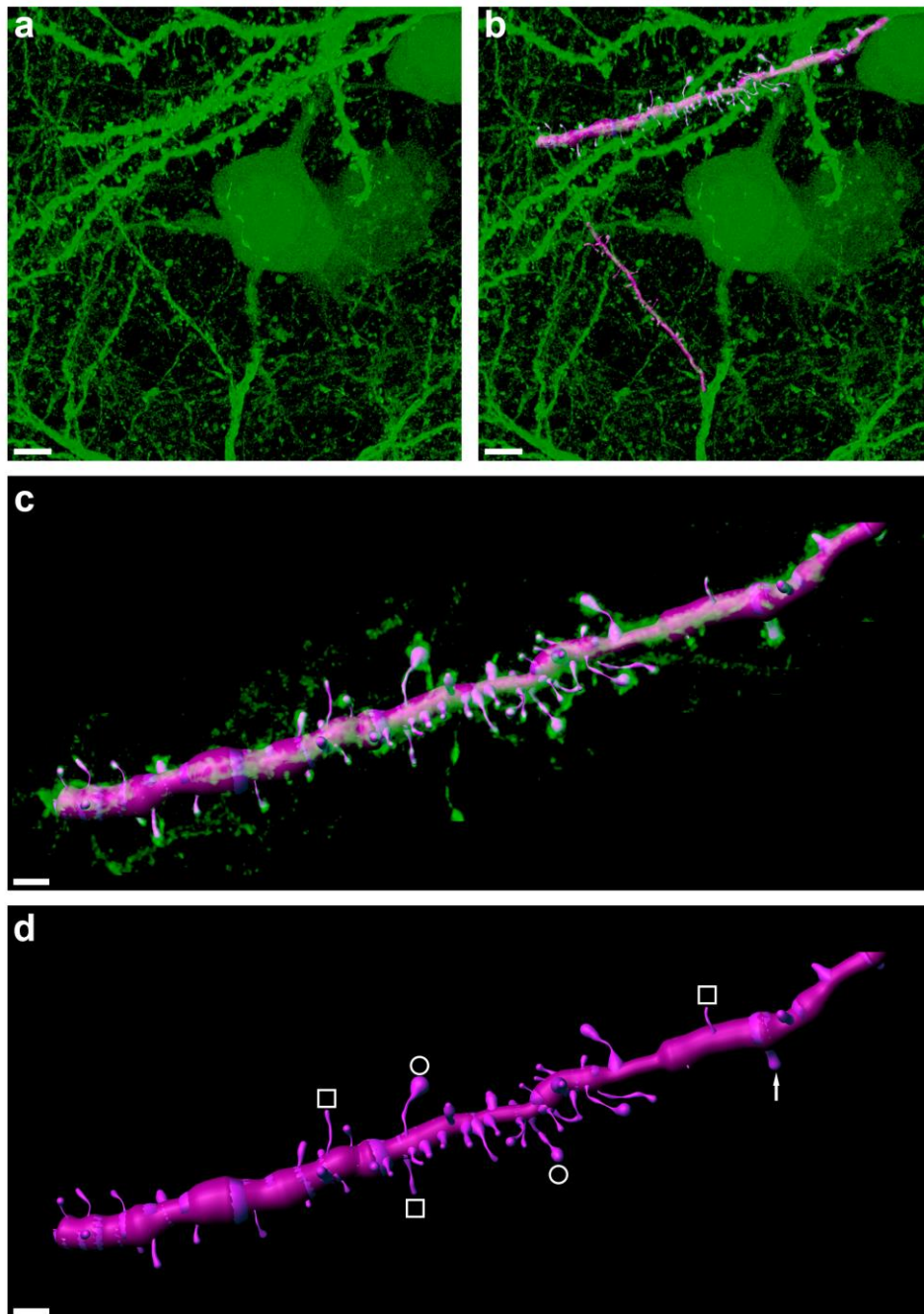
169 **Fig. 3 | Retrograde expression is restricted to neuronal cell types.** **a**, Confocal microscopy image
170 of zebra finch HVC with retrogradely labeled HVC_X neurons. **b**, Immunostaining with anti-HuC/HuD,
171 a commonly used antibody against neurons. **c**, Overlay of eGFP signal (green) and HuC/HuD signal
172 (magenta), showing no HVC_X neurons unlabeled for HuC/HuD. **d**, **e**, **f**, Higher magnification of the
173 boxed regions in **a**, **b**, **c**. Scale bars **a**, **b**, **c**, 100 μ m; **d**, **e**, **f**, 20 μ m.

174

175 Visualization of morphological details in retrogradely labeled projection neurons

176 The weak transgene expression produced by previous retrograde vectors for songbirds typically
177 results in fluorescent protein-labeling that is often limited to somata and small extensions of proximal
178 neurites^{9,13}. Using our new eGFP-construct thus opens new possibilities for highly detailed
179 morphological analysis of songbird projection neurons. In fact, the high expression levels of eGFP in
180 HVC_X neurons 7 days post-delivery allowed a remarkable visualization of dendritic morphological
181 details. Adjacent to imaged dendrites, we found clearly distinguishable dendritic spines throughout
182 HVC (Fig. 1e), at sufficient detail to distinguish and trace different spine types (Fig. 4).

183 The extensive eGFP labeling makes our construct a promising candidate for *in vivo* imaging of
184 morphological plasticity. To date, *in vivo* imaging of dendritic spine plasticity in songbirds has been
185 achieved exclusively via lentivirus-mediated fluorescence labeling^{12,26}, a tool that lacks retrograde
186 transduction capabilities. Furthermore, the strong eGFP expression we demonstrate is highly
187 beneficial for tissue processing techniques that require a strong initial fluorophore expression,
188 including large-volume expansion (lattice) light-sheet microscopy (ExLSM²⁷, ExLLSM²⁸) and
189 whole-brain tissue clearing²⁹.



191 **Fig. 4 | Strong eGFP expression permissive for reconstructing dendritic spine morphologies.** **a,**
192 High magnification confocal image stack of retrogradely labeled HVC_X neurons showing strong
193 expression of eGFP in dendritic fragments. **b,** Digital 3D-reconstruction (magenta overlay) of two
194 exemplary dendritic fragments. **c,** Isolated and zoomed view of the upper dendritic fragment shown
195 in **b,** revealing high morphological detail. **d,** In the semi-automatically reconstructed dendritic
196 fragment, various spine morphologies can be recognized including filopodia (white squares),
197 mushroom heads (white circles), and stubby spines (white arrow). Scale bars **a, b,** 5 μm ; **c, d,** 2 μm .
198

199 **Retrograde expression in dopaminergic projection neurons**

200 Similarly to the mammalian basal ganglia, Area X is densely innervated by dopaminergic neurons of
201 the ventral tegmental area-substantia nigra pars compacta complex (VTA/SNc), forming a continuous
202 group of cells with diverse projection targets and innervation³⁰. In humans, the comparable
203 dopaminergic system is crucially affected by neurodegenerative disorders such as Parkinson's
204 disease³¹. Songbird VTA/SNc_X neurons (traditionally referred to as VTA_X neurons) play crucial roles
205 in vocal learning, as they are responsible for encoding reward prediction errors associated with
206 singing³².

207 In birds injected with our construct into Area X, we observed good retrograde eGFP labeling of
208 VTA/SNc_X neurons. To identify the types of the labeled neurons, we immunolabeled histological
209 sections for tyrosine hydroxylase (TH), which is a good marker for dopamine and has been shown to
210 label the majority of VTA/SNc_X neurons (estimates ranging from 88 to 95% of VTA/SNc_X
211 neurons)^{11,14,33}. We found that the majority of examined VTA/SNc_X neurons were indeed positively
212 labeled for TH (n=4 birds, Fig. 1h-k), suggesting that these neurons are dopaminergic.

213 The strength of retrograde labeling of dopaminergic VTA/SNc projection neurons in zebra finches
214 led us to investigate whether high labeling efficiency can also be observed in rodents. One of the most
215 effective retrograde vectors in rodents, AAV-retro, only poorly transduces mouse dopaminergic
216 projection neurons in the SNc³⁴. Coincidentally, we tested AAV-retro and found this construct to also
217 be non-functional in zebra finches (n=4 adult male zebra finches, single injections into Area X in both
218 hemispheres of the construct scAAV-2-retro-hCMV-I/E-chI-eGFP-p(A), with post-delivery

219 incubation times of 6 weeks). When we injected our eGFP-construct into the striatum of mice, a major
220 projection target of the SNc, we found successful labeling of dopaminergic SNc projection neurons
221 (confirmed with TH-immunolabeling, n=5 mice, Fig. 11-o).

222

223 **Retrograde expression in canary projection neurons**

224 The strong expression and retrograde transport of our new viral construct in both zebra finches and
225 mice hints towards a broad species applicability of this vector. We therefore sought to test our
226 construct on canaries. Canaries (*Serinus canaria*) are seasonal breeding songbirds that produce highly
227 complex and flexible songs with extremely fast syllable repetitions, making this species a valuable
228 model system for complex motor skill learning³⁵. Additionally, canaries are a popular model for sex
229 hormone-induced neuroplasticity³⁶. Seasonal changes in singing behavior in this species are
230 correlated with sex hormone fluctuations and striking neural changes. To date, the application of viral
231 vectors in the canary brain has been limited to the use of lentiviruses³⁷, which do not retrogradely
232 transduce projection neurons. Injections of our eGFP-construct into canary Area X resulted in strong
233 eGFP expression in HVC_X neurons 7 days after injection, confirming the rapid expression times
234 observed in zebra finches (Fig. 1f,g).

235

236 **Brainbow labeling of projection neuron target circuits**

237 One common problem associated with studying the structure of local neural circuits is excessive
238 labeling density, which can hinder the visual separation of adjacent neurons and their respective
239 dendrites. One tool that can potentially overcome this problem is brainbow labeling³⁸. Brainbow
240 labeling color-codes neurons via the relative expression ratios of diverse fluorescent proteins. One
241 brainbow technique achieves diverse labeling colors via the selective uptake ratios of diverse viral
242 particle types. This technique involves simply mixing and co-injecting three individual vector types

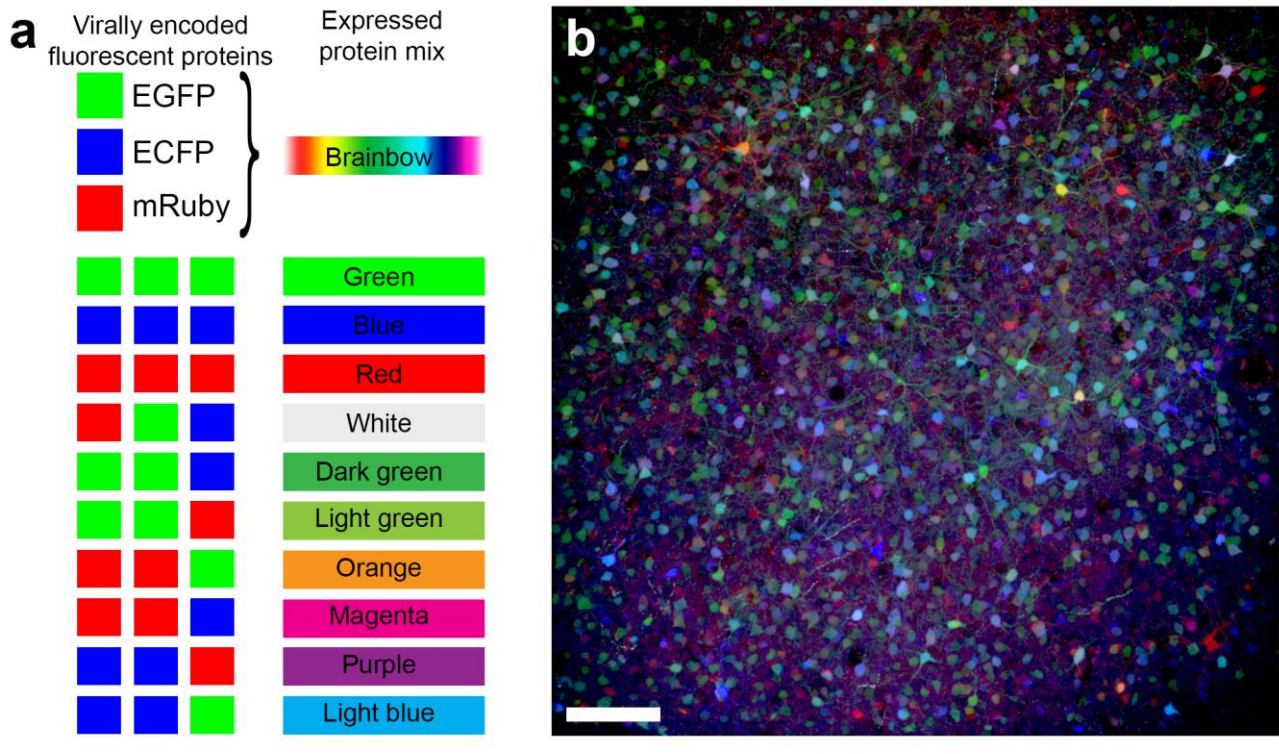
243 encoding different chemical tags or fluorophores³⁹ (Fig. 5a). Brainbow labeling in any of its variants
244 has not yet been applied in songbirds.

245 In addition to the eGFP-expressing vector, we produced two additional vectors expressing spectrally
246 distinct fluorescent proteins, enhanced cyan fluorescent protein (eCFP) and red fluorescent protein
247 (mRuby3). Next, we injected the three aforementioned constructs in a ratio of 1:1:1 into Area X of
248 adult male zebra finches. Local expression within Area X produced spectrally diverse neuron labeling
249 (Fig. 5b) with consistent and dense fluorophore expression patterns throughout neurons including
250 morphological fine structures such as spines (Fig. 5c). Although abundant brainbow labeling
251 strategies exist for mice, we are not aware of any AAV-based retrograde labeling strategy which does
252 not involve Cre-Lox recombination. We injected our eGFP-, eCFP-, and mRuby3-constructs in a ratio
253 of 1:1:1 into the murine area CA1 of the dorsal hippocampus (n=4). The injection of these three
254 constructs produced spectrally diverse labeling of projection neurons in the mouse entorhinal cortex
255 (Fig. 5d).

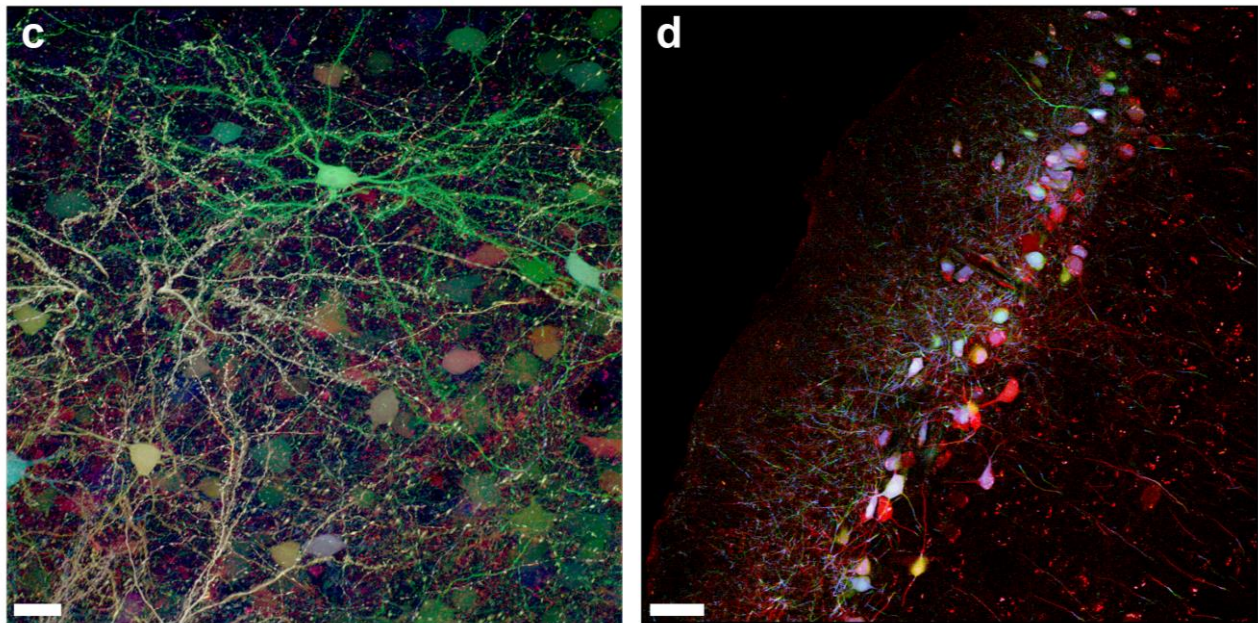
256

257

258



259



260

261 **Fig. 5 | Brainbow labeling in zebra finch and mouse.** **a**, AAV-mediated brainbow labeling is
262 achieved by injecting a mixture of three individual vectors encoding either eGFP, eCFP or mRuby3.
263 Each neuron ends up displaying a distinct color because of variable transduction of the three
264 fluorescent proteins, largely depending on the number of vectors per cell per fluorophore.
265 **b**, Brainbow labeling of locally transduced Area X neurons allows for recognition of individual
266 neurons in a densely labeled z-stack. **c**, High magnification confocal imaging reveals consistent color
267 labeling in dendritic fragments of Area X neurons, including spines. **d**, Retrograde brainbow labeling
268 of hippocampal projection neurons in mouse. Scale bars **b**, 100 μm ; **c**, 20 μm ; **d**, 50 μm .

269

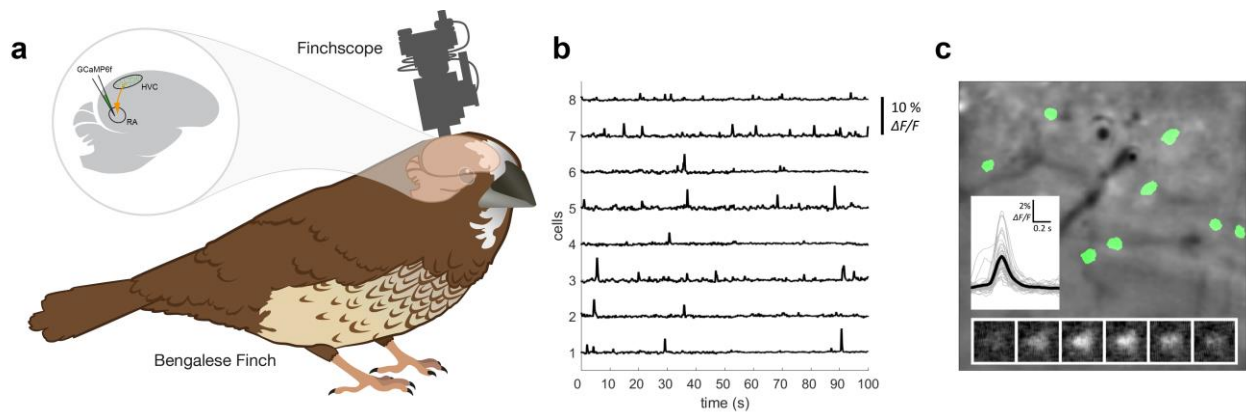
270 **Retrograde expression of calcium sensors**

271 In light of the obvious benefits of our construct for visualization of projection neuron circuits, we
272 sought to investigate whether the expression of other genetic cargo could be mediated equally well.
273 The packaging capacity of natural AAV serotypes is limited to a genome size of about 4.7 kb.
274 Nevertheless, the absolute packaging limit of AAV vectors has been challenged and one recent study
275 found a brick-wall limit of 5.2 kb for AAV-8⁴⁰. Because the maximum packaging size of an AAV
276 likely also depends on the exact protein composition of the nucleocapsid, we decided to produce the
277 same viral construct for GCaMP6f, with a total genome size of 5.286 kb, which is just over the
278 reported maximum. Production was successful and yielded a physical viral titer of 5.9×10^{12} vg/ml,
279 which seemed promising to test for *in vivo* calcium imaging.

280 GCaMP is a genetically encoded calcium (Ca^{2+}) sensor⁴¹ consisting of a circular GFP, calmodulin
281 (CaM) and a peptide chain (M13), which in its natural conformation shows only poor fluorescence.
282 In the presence of Ca^{2+} , CaM undergoes a structural change that entails a rapid increase in
283 fluorescence. GCaMP6f was engineered for fast fluorescence dynamics and high Ca^{2+} sensitivity,
284 resulting in reliable single-spike detection at 50-75 ms inter-spike intervals⁴².

285 We injected our GCaMP6f-construct into the RA of Bengalese finches (*Lonchura striata var.*
286 *domestica*), a further songbird species commonly used in birdsong research. We used a custom-built
287 miniaturized fluorescence microscope (see Methods) to image neuronal activity *in vivo* under
288 isoflurane anesthesia. We imaged spontaneous activity in HVC_{RA} neurons (Fig. 6, Supplementary
289 Video 1), an HVC projection neuron population that generates precise temporal sequences⁴³ during
290 song production. In a field of view of $(262.5 \mu\text{m})^2$, we were able to detect 48 spiking events in 8
291 distinct HVC_{RA} projection neurons over a time course of 100 s.

292



293

294 **Fig. 6 | *In vivo* calcium imaging in retrogradely labeled Bengalese finch RA-projecting (HVC_{RA})**
295 **neurons. a**, Schematic of the scAAV-2-DJ/9-hCMV-I/E-chI-GCaMP6f -p(A) injection site and
296 miniature microscope (finchscope) attachment in Bengalese finches. **b**, Fluorescence intensity traces
297 ($\Delta F/F$) for eight individual cells expressing GCaMP6f. All cells show clear spontaneous spike-like
298 activity as indicated by a sudden increase in signal intensity. **c**, Single frame of *in vivo* calcium
299 fluorescence movie under isoflurane anesthesia. Regions tracked over time are indicated in green.
300 Bottom inset shows fluorescence signal of one cell over a period of 0.5 s (100 ms between snapshots).
301 Left inset shows mean calcium transient (n=43) in black and individual transients in grey (windows
302 containing multiple events were excluded for visual clarity).

303

304

305

306

307

308

309

310

311

312

313

314

315 **Discussion**

316 We present a new viral construct for retrograde delivery of genetic cargo to projection neuron circuits
317 in songbirds, with fast and robust transgene expression and high transduction efficiency. Our
318 construct, scAAV-2-DJ/9-hCMV-I/E-chI-transgene-p(A), is suitable for studying the detailed
319 connectivity and function of songbird corticostriatal and vocal motor pathways essential for vocal
320 learning. Our construct also provides reliable access to probe the structure of cortical and
321 dopaminergic projection neuron circuits in both songbirds and mice. These findings indicate the
322 applicability of our new vector in both species and circuits that appear to be resistant to retrograde
323 targeting with AAV vectors.

324 The current lack of reliable tools to target specific neuron populations in songbirds has been a possible
325 contributor to the underrepresentation of songbirds as model species in medical and applied research.
326 For targeted manipulations of projection neuron populations in the zebra finch, one serotype, AAV-9,
327 has previously been used^{9-11,13}. However, these vectors entail significant drawbacks, such as low
328 transduction success rates, prolonged incubation times, and sparse and weak transgene expression,
329 all of which limit their application. These limitations were not remedied by the use of the presumably
330 stronger-expressing self-complementary variant of AAV-9^{9,13}, nor by exploiting the cre-flex system
331 with the cre-recombinase vector injected at the projection target^{10,11,13}. Unlike in songbirds, in mice,
332 the cre-flex system is very efficient and extremely low levels of cre are able to drive expression of
333 otherwise silenced transcripts⁴⁴.

334 Despite previous limitations as retrograde tools for the songbird brain, AAV vectors still seemed
335 worth exploration thanks to their extensive capsid variety, with more than 100 existing capsid variants.
336 The inability of certain viral vectors to infect songbird tissue is likely owed to diverse factors. Such
337 factors possibly include incompatibility of co-receptors for cellular access of the viral vector, as well
338 as differences in promoter sequences and intracellular physiology, both of which can impair
339 transduction. A further potential limiting factor is a substantially different immune response in birds
340 compared to mammals. Commonly, immune defense systems pose the first barrier when exploring

341 viral tools. Accordingly, the low transduction success rate of AAV-9 vectors hints towards a possible
342 strong immune response in zebra finches against this serotype. This hypothesis led us to explore
343 serotypes focusing on low immune response, which is a trait of vectors engineered for human gene
344 therapy. Human gene therapy vectors are required to have high transduction efficiency and low
345 immunogenicity, both of which were highly desirable characteristics for the new songbird viral tool
346 we were pursuing.

347 AAV serotypes have previously been selected in order to yield high efficiency and low
348 immunogenicity¹⁷. The single prevailing capsid, the AAV2, 8 & 9 chimera termed AAV-DJ, showed
349 superior transduction characteristics, which motivated us to test this capsid. We found that the
350 self-complementary variant of AAV-DJ shows great local expression in songbird brain tissue, with
351 great transduction characteristics, but unfortunately shows no retrograde transduction. Although
352 showing some potential for retrograde access to projection neurons^{34,45,46}, AAV vectors are
353 traditionally not used for retrograde studies. One notable exception, the AAV-retro construct, has
354 demonstrated a 10-fold higher retrograde transduction efficiency than AAV-DJ³⁴. This motivated us
355 to test AAV-retro, but we found this construct to be non-functional in zebra finches. We thus carefully
356 examined the changes introduced in AAV-retro, which presumably led to increased efficacy of
357 retrograde access. The critical changes appear to interact with the heparin sulfate proteoglycans
358 (HSPG) binding domain (HBD)⁴⁷. The 10-mer insert between positions 587 and 588 (Fig. 1a)
359 probably both disrupts HBD's functionality, as demonstrated by the reduced heparin binding affinity
360 of AAV-retro, and creates a new binding surface, which might improve vesicular trafficking or nuclear
361 entry of viral particles³⁴. Interestingly, the characteristics of the HBD were also carefully examined
362 by the creators of the AAV-DJ construct¹⁷. One of their negative controls produced for comparison to
363 AAV-DJ, AAV-DJ/9, included two point mutations in the HBD that disrupt heparin binding. These
364 two point mutations seemed to reduce transduction efficiency of AAV-DJ/9 in comparison to AAV-
365 DJ, but surprisingly also induced faster transduction kinetics. Faster transduction kinetics was a
366 highly desirable characteristic for the new songbird viral tool we were pursuing, which peaked our

367 interest in the AAV-DJ/9 capsid variant. Coincidentally, the point mutations of the HBD in AAV-DJ/9
368 also rendered this serotype closer to its parental serotype AAV-9¹⁷ (Fig. 1a), which has been shown
369 to have some potential for retrograde access in songbirds^{10-12,14}.

370 The exact composition of our construct combines many features that most likely all contribute
371 constitutively to the highly efficient transgene expression and retrograde transport (Fig. 1a,b). Clearly,
372 the AAV-DJ/9 capsid structure of the HBD plays a major role for the viral access through axon
373 terminals and the fast transduction kinetics. Nonetheless, this feature alone does not guarantee strong
374 retrograde expression. The viral vector also needs to be transported by the transduced cells lysosomal
375 system into the nucleus, where the genetic cargo has to be translated into messenger RNA (mRNA).
376 The process of conversion into mRNA in the nucleus can be drastically accelerated by packaging two
377 complementary copies of single stranded DNA genomes in a self-complementary AAV vector instead
378 of single stranded DNA genomes. However, self-complementary AAV vectors have also been shown
379 to induce a stronger immune response⁴⁸. When applying a self-complementary AAV9-based vector
380 (scAAV9) for retrograde access in songbirds, the self-complementary genome seems to neither have
381 improved transduction success rates, transduction efficiency, nor expression kinetics⁹. The
382 disappointing results obtained with scAAV9 might, however, be partially explained by the chosen
383 promoter. Although a wide range of promoters have been applied to songbird brain tissue, we are not
384 aware of a promoter that stands out in projection neurons. The scAAV9 vector has been employed in
385 songbirds using a CBh promoter⁹, a hybrid variant of the chicken beta actin (CBa) promoter.
386 Nonetheless, CBh supposedly ensures strong expression through self-complementary vector
387 mediated transduction in neuron types that are also affected by CMV promoters⁴⁹. Given the poor
388 transduction efficiency of scAAV-9-CBh, it could be that the hCMV immediate-early enhancer
389 (hCMV-I/E) and/or the chimeric intron (chI) of our self-complementary construct play crucial roles
390 for retrograde transduction in projection neurons. The introduced intron might contribute to the
391 improved transduction efficiency by regulating splicing of mRNA within the nucleus, which has been
392 shown to improve nuclear export⁵⁰. Further investigations would be necessary to fully elucidate the

393 exact contributions of individual components to retrograde transport and transduction efficiency and
394 kinetics.

395 In this work we present a new viral construct for excellent access to specific projection neuron
396 populations in songbirds. We demonstrated the suitability of our new construct for *in vivo* imaging of
397 calcium activity (Fig. 6), and for detailed morphological analysis based on extensive axonal and
398 dendritic labeling, using both single (Fig. 4) and multi-color approaches (Fig. 5). The high
399 transduction success rates and great transduction efficiency hint at the potential for this tool to make
400 a significant contribution to animal welfare by reducing the number of experimental animals required
401 in future studies, as stated by the 3R principles. Moreover, our new tool will likely open new avenues
402 of investigation into the structure and function of projection neuron populations and allow the study
403 of the brain circuits underlying vocal learning in unprecedented detail, including relevant
404 dopaminergic inputs during song development.

405

406

407

408

409

410

411 **Acknowledgments**

412 This work was supported by European Union's Horizon 2020 Marie Skłodowska-Curie grant Nr.
413 750055 (D.D.), ETH grants ETH-42 15-1 and ETH-20 19-01 (R.H. and B.G.), SNSF Sinergia grant
414 CRSII5-173721 (B.G.), and Swiss Data Science Center Grant C17-18 (B.G.). Part of the imaging was
415 performed at the Center for Microscopy and Image Analysis, University of Zurich. Some figures were
416 generated with the help of the Scientific Illustration and Visual Communication (SIVIC) center of the
417 University of Zurich. The AAV-DJ/9 helper plasmid was a kind gift from Mark A. Kay (Department
418 of Pediatrics & Genetics, Stanford University). The plasmid pBV1 was a kind gift from Bernd Vogt
419 (Institute of Virology, University of Zurich). We thank Veronika Bednarova and Benedikt Grothe
420 (Max-Planck Institute of Neurobiology) for preliminary experiments in mice.

421

422 **Author contributions**

423 DD, RH and FD conceived of the study. JC, MR, and DD designed viral constructs. JC and MR
424 produced all vectors. DD, FD, MDR, RT, CM, and RB performed experiments. DD, FD, and RK
425 contributed to confocal imaging. All authors contributed to image interpretation and data analysis.
426 MG, KO, RH, BG, RK, and JC provided equipment, reagents and materials. DD prepared all figures.
427 DD and MDR wrote the manuscript. All authors contributed to manuscript writing or revision and
428 approved of the final version.

429

430 **Declaration of Interests**

431 The authors declare no conflict of interests.

432

433 **Supplementary Files**

434

435 **Supplementary Video 1 | *In vivo* calcium imaging in retrogradely labeled HVC_{RA} neurons in the**
436 **Bengalese finch.** Video showing retrogradely transduced HVC_{RA} neurons expressing GCaMP6f
437 (bright spots). Eight cells show clear activity as indicated by the change in local signal intensity
438 (compare also to Fig. 6).

439

440 **References**

441

- 442 1. Rosenbaum, S. & Simon, P. *Speech and language disorders in children: Implications for the*
443 *Social Security Administration's Supplemental Security Income Program.* (The National
444 Academies Press, 2016). doi:10.17226/21872
- 445 2. Rapin, I. & Dunn, M. Update on the language disorders of individuals on the autistic
446 spectrum. *Brain Dev.* **25**, 166–72 (2003).
- 447 3. Tirosh, E. & Cohen, A. Language deficit with attention-deficit disorder: a prevalent
448 comorbidity. *J. Child Neurol.* **13**, 493–7 (1998).
- 449 4. Mayes, A. K., Reilly, S. & Morgan, A. T. Neural correlates of childhood language disorder: a
450 systematic review. *Dev. Med. Child Neurol.* **57**, 706–17 (2015).
- 451 5. Hauser, M. D., Chomsky, N. & Fitch, W. T. The faculty of language: what is it, who has it,
452 and how did it evolve? *Science* **298**, 1569–79 (2002).
- 453 6. Bolhuis, J. J., Okanoya, K. & Scharff, C. Twitter evolution: converging mechanisms in
454 birdsong and human speech. *Nat. Rev. Neurosci.* **11**, 747–759 (2010).
- 455 7. Callaway, E. M. Transneuronal circuit tracing with neurotropic viruses. *Curr. Opin.*
456 *Neurobiol.* **18**, 617–623 (2008).
- 457 8. Larsen, D. D., Wickersham, I. R. & Callaway, E. M. Retrograde tracing with recombinant
458 rabies virus reveals correlations between projection targets and dendritic architecture in layer
459 5 of mouse barrel cortex. *Front. Neural Circuits* **1**, (2008).
- 460 9. Chen, R. *et al.* Songbird Ventral Pallidum Sends Diverse Performance Error Signals to
461 Dopaminergic Midbrain. *Neuron* **103**, 266-276.e4 (2019).
- 462 10. Daliparthi, V. K. *et al.* Transitioning between preparatory and precisely sequenced neuronal
463 activity in production of a skilled behavior. *Elife* **8**, 1–26 (2019).
- 464 11. Hisey, E., Kearney, M. G. & Mooney, R. A common neural circuit mechanism for internally
465 guided and externally reinforced forms of motor learning. *Nat. Neurosci.* **21**, 589–597
466 (2018).
- 467 12. Roberts, T. F., Gobes, S. M. H., Murugan, M., Ölveczky, B. P. & Mooney, R. Motor circuits
468 are required to encode a sensory model for imitative learning. *Nat. Neurosci.* **15**, 1454–1459
469 (2012).
- 470 13. Roberts, T. F. *et al.* Identification of a motor-to-auditory pathway important for vocal
471 learning. *Nat. Neurosci.* **20**, 978–986 (2017).
- 472 14. Xiao, L. *et al.* A Basal Ganglia Circuit Sufficient to Guide Birdsong Learning. *Neuron* **98**,
473 208-221.e5 (2018).
- 474 15. Tanaka, M., Sun, F., Li, Y. & Mooney, R. A mesocortical dopamine circuit enables the
475 cultural transmission of vocal behaviour. *Nature* **563**, 117–120 (2018).
- 476 16. Mooney, R. Neural mechanisms for learned birdsong. *Learn. Mem.* **16**, 655–669 (2009).
- 477 17. Grimm, D. *et al.* In vitro and in vivo gene therapy vector evolution via multispecies
478 interbreeding and retargeting of adeno-associated viruses. *J. Virol.* **82**, 5887–911 (2008).
- 479 18. Mooney, R. Auditory–vocal mirroring in songbirds. *Philos. Trans. R. Soc. B Biol. Sci.* **369**,
480 20130490 (2014).
- 481 19. Roberts, T. F., Klein, M. E., Kubke, M. F., Wild, J. M. & Mooney, R. Telencephalic neurons
482 monosynaptically link brainstem and forebrain premotor networks necessary for song. *J.*
483 *Neurosci.* **28**, 3479–3489 (2008).
- 484 20. Dutar, P., Vu, H. M. & Perkel, D. J. Multiple cell types distinguished by physiological,
485 pharmacological, and anatomic properties in nucleus HVC of the adult zebra finch. *J.*
486 *Neurophysiol.* **80**, 1828–1838 (1998).
- 487 21. Di Filippo, M. *et al.* Short-term and long-term plasticity at corticostriatal synapses:
488 implications for learning and memory. *Behav. Brain Res.* **199**, 108–18 (2009).
- 489 22. Mandelblat-Cerf, Y., Las, L., Denisenko, N. & Fee, M. S. A role for descending auditory
490 cortical projections in songbird vocal learning. *Elife* **3**, 1–23 (2014).

- 491 23. Zingg, B. *et al.* AAV-Mediated Anterograde Transsynaptic Tagging: Mapping
492 Corticocollicular Input-Defined Neural Pathways for Defense Behaviors. *Neuron* **93**, 33–47
493 (2017).
- 494 24. Zhao, F. *et al.* Anterograde Trans-Synaptic Tagging Mediated by Adeno-Associated Virus.
495 *Neurosci. Bull.* **33**, 348–350 (2017).
- 496 25. Kornfeld, J. *et al.* EM connectomics reveals axonal target variation in a sequence-generating
497 network. *Elife* **6**, 1–20 (2017).
- 498 26. Roberts, T. F., Tschida, K. a, Klein, M. E. & Mooney, R. Rapid spine stabilization and
499 synaptic enhancement at the onset of behavioural learning. *Nature* **463**, 948–952 (2010).
- 500 27. Düring, D. N., Rocha, M. D., Dittrich, F., Gahr, M. & Hahnloser, R. H. R. Expansion Light
501 Sheet Microscopy Resolves Subcellular Structures in Large Portions of the Songbird Brain.
502 *Front. Neuroanat.* **13**, (2019).
- 503 28. Gao, R. *et al.* Cortical column and whole-brain imaging with molecular contrast and
504 nanoscale resolution. *Science (80-.)*. **363**, eaau8302 (2019).
- 505 29. Rocha, M. D. *et al.* Tissue Clearing and Light Sheet Microscopy: Imaging the Unsectioned
506 Adult Zebra Finch Brain at Cellular Resolution. *Front. Neuroanat.* **13**, (2019).
- 507 30. Gale, S. D., Person, A. L. & Perkel, A. D. J. A novel basal ganglia pathway forms a loop
508 linking a vocal learning circuit with its dopaminergic input. *J. Comp. Neurol.* **508**, 824–839
509 (2008).
- 510 31. Damier, P., Hirsch, E. C., Agid, Y. & Graybiel, A. M. The substantia nigra of the human
511 brain. *Brain* **122**, 1437–1448 (1999).
- 512 32. Gadagkar, V. *et al.* Dopamine neurons encode performance error in singing birds. *Science*
513 (80-.). **354**, 1278–1282 (2016).
- 514 33. Person, A. L., Gale, S. D., Farries, M. a. & Perkel, D. J. Organization of the songbird basal
515 ganglia, including area X. *J. Comp. Neurol.* **508**, 840–866 (2008).
- 516 34. Tervo, D. G. R. *et al.* A Designer AAV Variant Permits Efficient Retrograde Access to
517 Projection Neurons. *Neuron* **92**, 372–382 (2016).
- 518 35. Vellema, M. *et al.* Accelerated redevelopment of vocal skills is preceded by lasting
519 reorganization of the song motor circuitry. *Elife* **8**, 1–26 (2019).
- 520 36. Gahr, M. Hormone-dependent neural plasticity in the juvenile and adult song system: What
521 makes a successful male? *Ann. N. Y. Acad. Sci.* **1016**, 684–703 (2004).
- 522 37. Cohen, Y. *et al.* Hidden neural states underlie canary song syntax. *bioRxiv* 1–19 (2019).
523 doi:10.1101/561761
- 524 38. Lichtman, J. W., Livet, J. & Sanes, J. R. A technicolour approach to the connectome. *Nat.*
525 *Rev. Neurosci.* **9**, 417–422 (2008).
- 526 39. Sakaguchi, R., Leiwe, M. N. & Imai, T. Bright multicolor labeling of neuronal circuits with
527 fluorescent proteins and chemical tags. *Elife* **7**, 1–28 (2018).
- 528 40. Wu, Z., Yang, H. & Colosi, P. Effect of genome size on AAV vector packaging. *Mol. Ther.*
529 **18**, 80–6 (2010).
- 530 41. Nakai, J., Ohkura, M. & Imoto, K. A high signal-to-noise Ca²⁺ probe composed of a single
531 green fluorescent protein. *Nat. Biotechnol.* **19**, 137–141 (2001).
- 532 42. Chen, T.-W. *et al.* Ultrasensitive fluorescent proteins for imaging neuronal activity. *Nature*
533 **499**, 295–300 (2013).
- 534 43. Hahnloser, R. H. R., Kozhevnikov, A. A. & Fee, M. S. An ultra-sparse code underlies the
535 generation of neural sequences in a songbird. *Nature* **419**, 65–70 (2002).
- 536 44. Rothermel, M., Brunert, D., Zabawa, C., Diaz-Quesada, M. & Wachowiak, M. Transgene
537 Expression in Target-Defined Neuron Populations Mediated by Retrograde Infection with
538 Adeno-Associated Viral Vectors. *J. Neurosci.* **33**, 15195–15206 (2013).
- 539 45. Castle, M. J., Gershenson, Z. T., Giles, A. R., Holzbaur, E. L. F. F. & Wolfe, J. H. Adeno-
540 associated virus serotypes 1, 8, and 9 share conserved mechanisms for anterograde and
541 retrograde axonal transport. *Hum. Gene Ther.* **25**, 705–20 (2014).
- 542 46. Hollis II, E. R., Kadoya, K., Hirsch, M., Samulski, R. J. & Tuszynski, M. H. Efficient

- 543 Retrograde Neuronal Transduction Utilizing Self-complementary AAV1. *Mol. Ther.* **16**, 296–
544 301 (2008).
- 545 47. DiMattia, M. A. *et al.* Structural Insight into the Unique Properties of Adeno-Associated
546 Virus Serotype 9. *J. Virol.* **86**, 6947–6958 (2012).
- 547 48. Wu, T. *et al.* Self-complementary AAVs Induce More Potent Transgene Product-specific
548 Immune Responses Compared to a Single-stranded Genome. *Mol. Ther.* **20**, 572–579 (2012).
- 549 49. Gray, S. J. *et al.* Optimizing Promoters for Recombinant Adeno-Associated Virus-Mediated
550 Gene Expression in the Peripheral and Central Nervous System Using Self-Complementary
551 Vectors. *Hum. Gene Ther.* **22**, 1143–1153 (2011).
- 552 50. Valencia, P., Dias, A. P. & Reed, R. Splicing promotes rapid and efficient mRNA export in
553 mammalian cells. *Proc. Natl. Acad. Sci.* **105**, 3386–3391 (2008).
- 554
- 555

556 **Methods**

557

558 **Design of self-complementary adeno-associated virus vector plasmids**

559 Self-complementary adeno-associated virus (AAV) vector plasmids (pscAAV) were constructed as
560 previously described^{1,2}. Briefly, the terminal resolution site (trs) and the packaging signal
561 (D-sequence) from psub-2-CBA-WPRE^{3,4} were deleted by *Bal* I restriction digestion within the AAV
562 serotype 2 (AAV-2) 5' inverted terminal repeat (5'-ITR) resulting in the plasmid pscAAV-2-Δ3'-ITR.
563 Subsequently, the multiple cloning site (MCS) of pBluescript II SK (+) (Stratagene) together with the
564 AAV-2 3'-ITR and simian virus 40 late polyadenylation signal (SV40p(A)) containing fragment of
565 psub-2-CMV-WPRE³ were inserted into pscAAV-2-Δ3'-ITR, resulting in the plasmid pscAAV-2-
566 MCS-SV40p(A). In the AAV vector plasmids used here (Fig. 1b), the human cytomegalovirus
567 (hCMV) promoter/immediate-early enhancer (IE) of peGFP-N1 (Clontech) and the chimeric intron
568 (chI) of pSI (Promega) were inserted into pscAAV-2-MCS-SV40p(A) resulting in pscAAV-2-hCMV-
569 chI-SV40p(A).

570 The eGFP open reading frame (ORF) was amplified by PCR using pscAAV-2-hCMV-chI-floxedGFP
571 as the template DNA and primers 5'-ATACTAGTGCCACCATGGTGAGCAAGGGCG-3' (forward)
572 and 5'-TTGCGCGGCCGCTTACTTGTACAGCTCGTCCATG3' (reverse). Amplicons were *Spe*
573 *I/Not* I restriction digested and inserted into the *Spe* *I/Not* I restriction digested
574 pscAAV-2-hCMV-chI-floxedGFP to generate pscAAV-2-hCMV-chI-eGFP (eGFP vector plasmid).
575 For construction of the mRuby3 vector plasmid (pscAAV-2-hCMV-chI-mRuby3-SV40p(A)), the
576 mRuby3 ORF was amplified by PCR using Addgene #85146 as the template DNA and primers
577 5'-CATTACTAGTGTTTAAACACTCGAGGCTAGCGCCACCATGGTGTCTAAGG-3' (forward)
578 and 5'-TAGGCGCGCCTACGTACAATTGGGTACCTTACTTGTACAGCTCGTCCATG-3'
579 (reverse). The resulting PCR product was cut with *Spe*I and *Bsr*GI and inserted into the *Spe* *I* and
580 *Bsr*G *I* sites of the eGFP vector plasmid.

581 For construction of the eCFP vector plasmid (pscAAV-2-hCMV-chI-eCFP-SV40p(A)), the eCFP
582 ORF was isolated from plasmid pBV1 as *Nhe* *I/Sac* II fragment and inserted into the *Sac* II/*Spe* *I*
583 opened eGFP vector plasmid.

584 For construction of the GCaMP6f vector plasmid (pscAAV-2-hCMV-chI-GCaMP6f-SV40p(A)), the
585 GCaMP6f ORF was isolated by *Bgl* II/*Bst*B *I* restriction digest from
586 pssAAV-2-hSyn1-chI-GCaMP6f-WPRE-SV40p(A) (N-terminal part of GCaMP6f) and by *Bst*B

587 I/BssH II(blunt) restriction digest from pssAAV-2-hEF1a-dlox-GCaMP6f(rev)-dlox-WPRE-bGHp(A)
588 (C-terminal part of GCaMP6f) and inserted into the BsrG I(blunt)/Bgl II restriction digested pscAAV-
589 2-hCMV-chI-Lck_eGFP-SV40p(A) to generate pscAAV-2-hCMV-chI-GCaMP6f-SV40p(A)
590 (GCaMP6f vector plasmid).

591 The identity of all constructs was confirmed by Sanger DNA sequencing and restriction endonuclease
592 analyses.

593 Sequences of all viral vectors and their corresponding plasmids can be found in the repository of the
594 Viral Vector Facility of the University of Zurich and ETH Zurich (<https://www.vvf.uzh.ch/en.html>).

595

596 **Production, purification, and quantification of self-complementary (sc) AAV vectors**

597 Self-complementary (sc) AAV vectors were produced and purified as previously described^{4,5}. Briefly,
598 human embryonic kidney (HEK) 293 cells⁶ expressing the simian virus (SV) large T-antigen⁷ (293T)
599 were transfected by polyethylenimine (PEI)-mediated cotransfection of AAV vector plasmids
600 (providing the to-be packaged AAV vector genome, see above), the AAV helper plasmid pAAV-DJ/9;
601 pAAV-DJ/9 providing the AAV serotype 2 rep proteins and the cap proteins of AAV-DJ/9) and
602 adenovirus (AV) helper plasmids pBS-E2A-VA-E4³ (providing the AV helper functions) in a 1:1:1
603 molar ratio.

604 At 120 to 168 hours post-transfection, HEK 293T cells were collected and separated from their
605 supernatant by low-speed centrifugation. AAV vectors released into the supernatant were
606 PEG-precipitated over night at 4 °C by adding a solution of polyethyleneglycol 8000 (8% v/v in 0.5 M
607 NaCl), and completed by low-speed centrifugation. Cleared supernatant was discarded and the
608 pelleted AAV vectors resuspended in AAV resuspension buffer (150 mM NaCl, 50 mM Tris-HCl, pH
609 8.5). HEK 293T cells were resuspended in AAV resuspension buffer and lysed by Bertin's Precellys
610 Evolution homogenizer in combination with 7 ml soft tissue homogenizing CK14 tubes (Bertin). The
611 crude cell lysate was DENARASE (c-LEcta GmbH) treated (150 U/ml, 90 to 120 minutes at 37 °C)
612 and cleared by centrifugation (10 minutes at 17.000 g/4 °C). The PEG-precipitated (1 hour at 3500
613 g/4 °C) AAV vectors were combined with the cleared cell lysate and subjected to discontinuous
614 density iodixanol (OptiPrep™, Axis-Shield) gradient (isopycnic) ultracentrifugation (2 hours 15
615 minutes at 365'929 g/15 °C). Subsequently, the iodixanol was removed from the AAV vector
616 containing fraction by 3 rounds of diafiltration using Vivaspin 20 ultrafiltration devices (100'000
617 MWCO, PES membrane, Sartorius) and 1x phosphate buffered saline (PBS) supplemented with 1
618 mM MgCl₂ and 2.5 mM KCl according to the manufacturer's instructions. The AAV vectors were
619 stored aliquoted at -80 °C.

620 Encapsidated viral vector genomes (vg) were quantified using the Qubit™ 3.0 fluorometer in
621 combination with the Qubit™ dsDNA HS Assay Kit (both Life Technologies). Briefly, 5 µl of
622 undiluted (or 1:10 diluted) AAV vectors were prepared in duplicate. Untreated and heat-denatured
623 (5 minutes at 95 °C) samples were quantified according to the manufacturer's instructions. Intraviral
624 (encapsidated) vector genome concentrations (vg/ml) were calculated by subtracting the extraviral
625 (non-encapsidated; untreated sample) from the total intra- and extraviral (encapsidated and non-
626 encapsidated; heat-denatured sample). All AAV vectors used in this study had vector genome
627 concentrations between 3.8 x 10¹² vg/ml and 7.4 x 10¹² vg/ml.

628 Identity of encapsidated genomes were verified and confirmed by Sanger DNA-sequencing of
629 amplicons produced from genomic AAV vector DNA templates (identity check).

630

631 **Animals**

632 Zebra finches were obtained from breeding colonies in Zurich, Switzerland, or Seewiesen, Germany;
633 canaries from breeding colonies in Seewiesen, Germany; and Bengalese finches from breeding
634 colonies in the University of Tokyo, Japan. C57BL/6 mice were obtained from Charles River
635 Germany and housed in the LASC animal husbandry at the University of Zurich.

636 Animal handling and all experimental procedures were conducted following the ethical principles
637 and guidelines for animal experiments of Switzerland/Germany/Japan.

638

639 **Surgical procedure for viral vector delivery**

640 Birds were deeply anesthetized using an orally administered mixture of oxygen with 1-3% isoflurane
641 gas before being placed in a custom stereotaxic apparatus. After applying a topical anesthetic, a
642 vertical incision was made in the skin over the skull, and a small craniotomy was performed at
643 predetermined distances from the anatomical landmark lambda. For bi-lateral injections into Area X
644 the following stereotaxic coordinates were used relative to lambda: anterior-posterior-axis (AP) +5.4
645 mm, medial-lateral-axis (ML) 1.6 mm, and dorsal-ventral-axis (DV) -3.2 mm, with an approximately
646 85 degree earbar-beak angle. For bi-lateral injections into RA of Bengalese finches we used the
647 following coordinates relative to lambda: AP +5.1 mm, ML 2.0 mm, and DV -1.5 mm, with an
648 approximately 180-degree earbar-beak angle. Following the craniotomy at the target locations,
649 coordinates were confirmed by electrophysiological recordings using 1 M Ω tungsten sharp electrodes.
650 Subsequently, 200 nl of undiluted viral vector were injected into each hemisphere using glass pipettes
651 attached to either a Nanoject III (Drummond Scientific), with a constant flow rate of 1 nl per second,
652 or a custom built pressure injector with a similar flow rate. To avoid backflow of viral vector and
653 untargeted transduction, injection pipettes were raised about 200 μ m relative to the injection site after
654 content delivery and let sit for 5 minutes prior to ejection. Cranial holes were covered with quickcast,
655 and the incision site in the skin was closed with tissue glue.

656 Mice were deeply anesthetized with Ketamine (90 mg/kg body weight)/Xylazine (8 mg/kg body
657 weight), with buprenorphine (0.1 mg/Kg body weight, i.p.) given pre-emptive 20 minutes prior to
658 anesthesia. Once pedal-reflex was absent, mice were mounted into a stereotaxic frame (Kopf), and
659 300 nl of undiluted viral vector were injected unilaterally into the dorsal striatum (DS) or into area
660 CA1 of the dorsal hippocampus at a rate of 50 nl/min employing a 33G needle (nanofil 33 G, WPI)
661 in a 10 μ l syringe (nanofil, WPI) and a microinjector pump (WPI; UMP3 UltraMicroPump) directly
662 mounted to the stereotaxic manipulator. The needle was left in place for an additional 5 minutes after
663 the completed injection to avoid backflow of the viral vector. After the injection needle was removed,
664 the incision was sutured. Animals received analgesic treatment for 3 days after surgery. The following
665 stereotaxic coordinates were used relative to bregma: AP +1.0 mm, ML +1.8 mm, and DV -3.0 mm
666 for DS; and AP -2.0 mm, ML +1.5 mm, and DV -1.6 mm for CA1.

667

668 **Tissue preparation and immunohistochemistry**

669 After isoflurane overdose, birds were transcardially perfused with PBS followed by 4% PFA
670 (paraformaldehyde) in PBS (pH 7.4). Brains were extracted and post-fixed in 4% PFA overnight at
671 4 °C, stored in PBS, and hemisected. Hemispheres were sectioned into either 30 or 60 µm-thick
672 sagittal sections using a freezing sliding microtome (Leica Microsystems).

673 9 to 10 days after viral vector injection, mice were anesthetized with a lethal dose of Pentobarbital
674 (200 mg/kg, i.p.), and transcardially perfused with saline followed by 4% PFA. Brains were extracted
675 and post-fixed in 4 % PFA for 24 hours. Sections were prepared with a Vibratome (Leica
676 Microsystems) at 50 µm thickness.

677 Sections were either directly mounted onto glass slides with Vectashield antifade mounting medium
678 (Vector Laboratories) and coverslipped for imaging of native fluorescence signal, or subjected to
679 immunohistochemistry protocols, as described below.

680 Sections were washed with PBS, blocked in 10% normal goat serum/0.5% saponin/PBS for
681 90 minutes, and incubated overnight with primary antibodies in blocking solution at 4 °C. Sections
682 were then washed in 0.5% saponin/PBS, and incubated with secondary antibodies in blocking solution
683 for 3 hours at room temperature. Finally, sections were washed in 0.5% saponin/PBS, mounted onto
684 glass slides with Vectashield antifade mounting medium (Vector Laboratories), and coverslipped.

685 The following primary antibodies were used: chicken anti-GFP (1:1000, Aves, GFP-1020), mouse
686 anti-HuC/HuD (1:20, Invitrogen, A21271), and rabbit anti-TH (1:500, Millipore, AB152). The
687 following secondary antibodies were used: goat anti-chicken conjugated to Alexa Fluor 488 (1:500,
688 Abcam, ab150169), goat anti-mouse conjugated to Alexa Fluor 555 (1:500, Invitrogen, A21422), and
689 goat anti-rabbit conjugated to Alexa Fluor 555 (1:500, Invitrogen, A21428).

690

691 **Image acquisition and analysis**

692 Fluorescence images were acquired using a Leica SP8 confocal microscope (Leica Microsystems)
693 using the 488 nm (eGFP/Alexa Fluor 488) and 561 nm (Alexa Fluor 555) laser line for excitation,
694 and spectral windows of 493 nm - 550 nm and 566 nm - 650 nm respectively on hybrid detectors
695 (HyD) for signal detection. Low magnification images were acquired using a 20x/0.75 NA multi-
696 immersion objective (HC PL APO CS2) , and higher magnification images with a 63x/1.3 NA
697 glycerol-immersion objective (HCX PL APO CS2). Pixel resolution and z section distances were set
698 considering the nyquist criteria as defined at <https://svi.nl/NyquistCalculator> to ensure optimal post
699 processing results.

700 When imaging the entire HVC multiple field of views where imaged with a 10% overlap and merged
701 after acquisition using Leica's imaging software (LASX). Prior to analysis of image stacks recorded
702 with the higher magnification objective images were deconvolved using Huygens professional (SVI).
703 Spine reconstructions and density measurements were performed with Imaris 9.2.1 (Bitplane) using
704 the semi-automatic filament tracing function. Soma counts and densities were performed using Imaris'
705 spot tool with user defined thresholds. Sections for analysis were selected in a way that they roughly
706 represent the same anatomical location (i.e. similar medio-lateral positions), and we performed soma
707 counts in standardized volumes of 300 x 300 x 30 µm³ to accommodate for slight variations in HVC
708 size or section thickness.

709

710 **Calcium imaging**

711 A custom-built, miniaturized fluorescence microscope was used to capture the temporal dynamics of
712 calcium induced GFP signal from HVC projection neurons retrogradely transduced with our
713 GCaMP6f-construct. The miniaturized microscope (named “finchscope”) was built in-lab according
714 to the previously described manufacturing protocol⁸.

715 In order to image fluorescence signals, a cranial window was prepared in deeply anesthetized birds
716 (by oral administration of a mixture of oxygen with 1-3% isoflurane) as follows. The skull and dura
717 over HVC were removed, and a ~3 mm hole on the skull just above HVC was made using a dental
718 drill and scalpel. A round cover glass (3-mm diameter, CS-3R-0, Warner Instruments) was placed on
719 the brain surface and fixed to the skull with tissue adhesive (Gluture, World Precision Instruments).
720 The edge of glass window was secured to the skull with dental cement (PalaXpress, Kulzer). We then
721 recorded spontaneous calcium activity by placing the finchscope just above the glass window with a
722 stereotaxic manipulator.

723 Movies were recorded with the finchscope at 30 FPS and $(0.75 \mu\text{m})^2$ pixel size via a video capture
724 device (GV-USB2, I-O DATA) and a recording software (AMcap), and were processed with in-house
725 developed MATLAB (Mathworks) scripts as follows. First, we temporally smoothed each pixel using
726 a 5-frame moving average. Next, we removed wide field intensity fluctuations by dividing each frame
727 by a low-pass-filtered version of itself. For further analysis, we re-expressed each pixel in units of
728 relative changes in fluorescence, given by $\Delta F(t)/F_0 = (F(t) - F_0)/F_0$, where F_0 is the mean pixel value
729 calculated by averaging over the entire movie. To obtain activity traces and spatial filters
730 corresponding to the imaged cells, we applied an established automated signal extraction method to
731 the preprocessed movie⁹. Finally, we manually verified all extracted cells and discarded false
732 positives.

733

734

735 **References**

736

- 737 1. McCarty, D. M. *et al.* Adeno-associated virus terminal repeat (TR) mutant generates self-
738 complementary vectors to overcome the rate-limiting step to transduction in vivo. *Gene Ther.*
739 **10**, 2112–2118 (2003).
- 740 2. Wang, Z. *et al.* Rapid and highly efficient transduction by double-stranded adeno-associated
741 virus vectors in vitro and in vivo. *Gene Ther.* **10**, 2105–2111 (2003).
- 742 3. Paterna, J.-C., Moccetti, T., Mura, A., Feldon, J. & Büeler, H. Influence of promoter and
743 WHV post-transcriptional regulatory element on AAV-mediated transgene expression in the
744 rat brain. *Gene Ther.* **7**, 1304–1311 (2000).
- 745 4. Paterna, J.-C. J.-C., Feldon, J., Bueler, H. & Büeler, H. Transduction Profiles of Recombinant
746 Adeno-Associated Virus Vectors Derived from Serotypes 2 and 5 in the Nigrostriatal System
747 of Rats. *J. Virol.* **78**, 6808–17 (2004).
- 748 5. Zolotukhin, S. *et al.* Recombinant adeno-associated virus purification using novel methods
749 improves infectious titer and yield. *Gene Ther.* **6**, 973–985 (1999).
- 750 6. Graham, F. L., Smiley, J., Russell, W. C. & Nairn, R. Characteristics of a Human Cell Line
751 Transformed by DNA from Human Adenovirus Type 5. *J. Gen. Virol.* **36**, 59–72 (1977).
- 752 7. DuBridge, R. B. *et al.* Analysis of mutation in human cells by using an Epstein-Barr virus
753 shuttle system. *Mol. Cell. Biol.* **7**, 379–387 (1987).
- 754 8. Liberti, W. A., Perkins, L. N., Leman, D. P. & Gardner, T. J. An open source, wireless capable
755 miniature microscope system. *J. Neural Eng.* **14**, 045001 (2017).
- 756 9. Mukamel, E. A., Nimmerjahn, A. & Schnitzer, M. J. Automated Analysis of Cellular Signals
757 from Large-Scale Calcium Imaging Data. *Neuron* **63**, 747–760 (2009).

758

759